

Roton confinement in trapped dipolar Bose-Einstein condensates

M. Jona-Lasinio, K. Lakomy and L. Santos

Institut für Theoretische Physik, Leibniz Universität, 30167 Hannover, Germany

(Dated: April 5, 2013)

Roton excitations constitute a key feature of dipolar gases, connecting these gases with superfluid helium. We show that the density dependence of the roton minimum results in a spatial roton confinement, particularly relevant in pancake dipolar condensates with large aspect ratios. We show that roton confinement plays a crucial role in the dynamics after roton instability, and that arresting the instability may create a trapped roton gas revealed by confined density modulations. We discuss the local susceptibility against density perturbations, which we illustrate for the case of vortices. Roton confinement is expected to play a key role in experiments.

PACS numbers: 03.75.Kk 05.30.Jp and 67.85.-d

Dipolar gases have attracted a growing attention in recent years. Quantum degenerate gases of magnetic atoms as chromium [1], dysprosium [2] and erbium [3] have already been realized. Moreover, the preparation of heteronuclear molecules in their ro-vibrational ground-state [4] opens the path for the creation of a degenerate gas of polar molecules, a goal currently pursued by various groups worldwide [5]. Rydberg atoms provide yet another possible realization of a highly polar gas [6].

The rich physics of dipolar gases arises from dipole-dipole interactions (DDI) [7]. Dipolar Bose-Einstein condensates (dBECs) feature a geometry-dependent stability [8] and a peculiar dispersion of the elementary excitations. Nonpolar BECs present the usual Bogoliubov spectrum, with a linear (phonon) dispersion at low momenta, and a quadratic dispersion at large momenta [9]. Under proper conditions, dBECs present a dispersion minimum at intermediate momenta [10, 11] resembling the roton minimum of superfluid He [12].

Roton excitations are crucial in He, reducing the critical superfluid velocity [13] and leading to density modulations at defects [15–19]. Remarkably, similar effects have also been predicted in dBECs [14, 20–22]. Moreover, the roton minimum is crucial for the stability of a dBEC. When the minimum reaches zero energy, the dBEC becomes unstable against finite-momentum excitations (roton instability) [10, 11, 23], which differs fundamentally from the usual phonon instability.

Roton properties in He may be controlled by means of pressure [24]. Similarly, the roton minimum in dBECs depends on interactions and therefore on density. In this Letter we demonstrate that this density dependence leads to a spatial roton confinement in trapped dBECs. Roton confinement has been hinted in recent numerical calculations [14, 25] and resembles that of rotons at vortex lines in He [26]. We show that roton confinement is crucial to understand the roton instability in pancake traps. We also discuss how arresting the instability may create a trapped roton gas. We finally analyze other consequences of the roton confinement, such as local susceptibility against density perturbations.

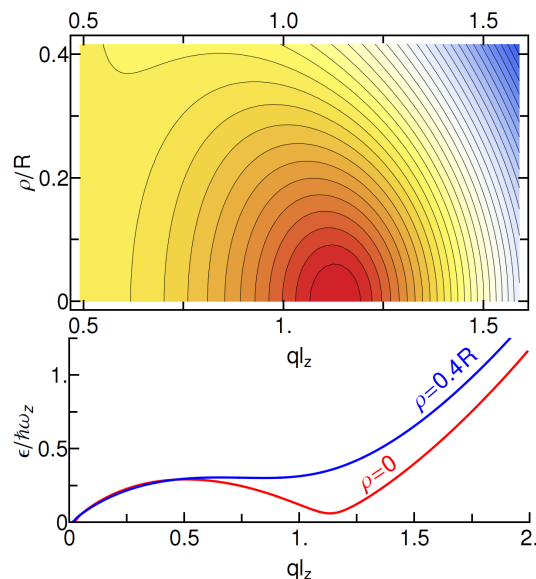


FIG. 1: (Color online) (Top) Local spectrum of a BEC of 2×10^5 Er atoms $\omega_z = 2\pi \times 1$ kHz and $\lambda = 40$. Note a minimum (dark red region in the top figure) in both space and momentum. (Bottom) Change of the roton minimum for two different radial positions.

We consider a dBEC of N bosons of mass m and (electric or magnetic) dipole moment d oriented along z . The dBEC is in a pancake harmonic trap $V_t(\mathbf{r})$ of frequencies ω in the xy plane and $\omega_z = \lambda\omega$ along z , with $\lambda \gg 1$. The dBEC wave function $\phi(\mathbf{r}, t)$ obeys the nonlocal Gross-Pitaevskii equation (GPE) [7],

$$i\hbar \frac{\partial}{\partial t} \phi(\mathbf{r}, t) = \left[-\frac{\hbar^2 \nabla^2}{2m} + V_t(\mathbf{r}) + g|\phi(\mathbf{r}, t)|^2 \right] \phi(\mathbf{r}, t) + \int d^3r' V_{dd}(\mathbf{r} - \mathbf{r}') |\phi(\mathbf{r}', t)|^2 \phi(\mathbf{r}, t), \quad (1)$$

where $g = 4\pi\hbar^2 a N/m$ characterizes the short-range interactions, a is the s -wave scattering length, $V_{dd}(\mathbf{r}) = \frac{Nd^2}{r^3}(1 - 3\cos^2\theta)$ is the DDI potential, θ is the angle between \mathbf{r} and the z axis, and $\int d^3r |\phi(\mathbf{r}, t)|^2 = 1$.

We first consider $\omega = 0$ [27], briefly summariz-

ing the results of Ref. [10]. The ground-state wavefunction is $\phi_0(z) \exp(-i\mu t/\hbar)$, where μ is the chemical potential and $\phi_0(z)$ fulfills a 1D local GPE with a regularized coupling constant $g + g_d$, with $g_d = 8\pi N d^2/3$. Assuming a transverse Thomas-Fermi (TF) profile $\phi_0(z) = \sqrt{n_0(1 - z^2/L^2)}$, with n_0 the peak density, one obtains $\mu = (g + g_d)n_0$. Excitations of energy ϵ are evaluated by substituting $\phi(\mathbf{r}, z, t) = e^{-i\mu t/\hbar} [\phi_0(z) + u(\mathbf{r}, z)e^{-i\epsilon t/\hbar} - v(\mathbf{r}, z)^* e^{i\epsilon t/\hbar}]$ (with $\mathbf{r} \equiv (x, y)$) into Eq. (1), and keeping only linear terms in u and v . The excitations have a defined in-plane momentum \mathbf{q} , and hence $f_{\pm}(\mathbf{r}, z) \equiv [u(\mathbf{r}, z) \pm v(\mathbf{r}, z)] = f_{\pm}(\mathbf{q})e^{i\mathbf{q}\cdot\mathbf{r}}$. The lowest eigenenergy obtained from the Bogoliubov-de Gennes (BdG) equations for each \mathbf{q} builds the dispersion $\epsilon(q)$. Interestingly, $\epsilon(q)$ may present a roton-like minimum at intermediate q . Assuming $qL \gg 1$ and $\mu E(q)|\beta - 2|/(\beta + 1) \lesssim \hbar^2\omega_z^2$ (with $\beta \equiv g_d/g$ and $E(q) \equiv \hbar^2 q^2/2m$) we obtain an approximate expression of the dispersion, $\epsilon_h^2(q, \mu) = E(q)^2 - G(\beta)E(q)\mu + \hbar^2\omega_z^2$, with $G(\beta) \equiv \frac{(\beta-2)(5\beta+2)}{3(1+\beta)(2\beta+1)}$, as well as the associated eigenstate, $f_+(z) \simeq \phi_0(z)$. The expression $\epsilon_h(q, \mu)$ agrees well with the numerical $\epsilon(q)$ and shows that the roton depth depends explicitly on μ and hence on density.

Interesting insights about the roton physics for $\omega > 0$ are provided by the concept of *local spectrum* $\epsilon(q, \rho)$, which we introduce here. We compute from Eq. (1) the ground-state $n_0(\mathbf{r}) = |\phi_0(\mathbf{r})|^2$, which in the TF regime is approximated by $n_0(\mathbf{r}) = \tilde{n}_0(1 - \rho^2/R^2 - z^2/L^2)$. We obtain for each ρ the z -profile $n_0^{1D}(z) = n_0(\mathbf{r})/\int dz n_0(\mathbf{r})$, and the *local* chemical potential $\mu_l(\rho)$. Solving the corresponding 1D BdG equations [10] we obtain $\epsilon_h(q, \mu_l(\rho))$, which approximates the local spectrum $\epsilon(q, \rho)$ consistently with the LDA. The local chemical potential $\mu_l(\rho)$ decreases quadratically with ρ , and hence at the trap center ($\rho = 0$) the roton energy is lowest: $\epsilon_r/\hbar\omega_z \equiv \epsilon(q = q_r, \rho = 0)/\hbar\omega_z \simeq \sqrt{1 - (G(\beta)\mu_l(0)/2\hbar\omega_z)^2}$. The local spectrum presents a minimum both in momentum, at $q_r l_z \simeq \sqrt{G(\beta)\mu_l(0)/\hbar\omega_z}$ (note that $q_r l_z \sim 1$, with $l_z \equiv \sqrt{\hbar/m\omega_z}$, see [10]), and in space, at $\rho = 0$ (Fig. 1). For larger ρ the minimum becomes shallower and eventually disappears. Hence, remarkably, the inhomogeneous BEC density results in a spatial *roton confinement*. Around the minimum:

$$\epsilon(q, \rho) \simeq \epsilon_r + \frac{\hbar^2(q - q_r)^2}{2m_*} + \frac{1}{2}m_*\omega_*^2\rho^2. \quad (2)$$

where the effective roton mass $m_* \equiv m\sqrt{1/(q_r l_z)^4 - 1/4}$ and the effective harmonic frequency $\omega_* \equiv \omega_z \frac{mq_r l_z^2}{m_* R\sqrt{2}}$, define the roton localization length $l_* \equiv \sqrt{\hbar/m_*\omega_*} = 2^{1/4}(R/q_r)^{1/2}$. Note that $l_*/R \sim \sqrt{l_z/R}$, and hence $l_* \ll R$ for $\lambda \gg 1$. Moreover, $q_r l_* \sim \sqrt{R/l_z} \gg 1$ if $\lambda \gg 1$, which justifies the use of LDA above.

We now calculate the localized roton wave functions using the LDA and the formalism of Ref. [10]. Assuming

$l_* \ll R$, we approximate $f_+(\mathbf{r}, z) \simeq F(\mathbf{r})\phi_0(\mathbf{r}, z)$, where $F(\mathbf{r})$ has a narrow momentum distribution $\tilde{F}(\mathbf{q})$ centered around q_r with a width $\delta q \propto 1/l_* \ll q_r$. The finite width of $\tilde{F}(\mathbf{q})$ must be now considered and as a result $\tilde{F}(\mathbf{q})$ fulfills the eigenvalue equation $\epsilon^2 \tilde{F}(\mathbf{q}) \simeq [\epsilon_r + \hat{H}]^2 \tilde{F}(\mathbf{q})$, with $\hat{H} \equiv \frac{\hbar^2}{2m_*}(q - q_r)^2 - \frac{1}{2}m_*\omega_*^2\nabla_{\mathbf{q}}^2$. Interestingly, \hat{H} resembles the Hamiltonian of a trapped BEC in the presence of spin-orbit coupling [29, 30], where the Rashba-like dispersion $\sim (q - q_r)^2$ acts as a ring-like potential in \mathbf{q} -space. The eigenfunctions of \hat{H} , $\eta_{n,s}(\mathbf{q})e^{is\varphi}/\sqrt{q}$, fulfill

$$\left[\frac{E_{n,s}}{\hbar\omega_*} - \frac{s^2 - \frac{1}{4}}{2(q l_*)^2} \right] \eta_{n,s} = \left[-\frac{1}{2l_*^2} \frac{d^2}{dq^2} + \frac{l_*^2}{2}(q - q_r)^2 \right] \eta_{n,s}. \quad (3)$$

For $q_r l_* \gg 1$, we expand around $q \simeq q_r$, obtaining the eigenenergies $E_{n,s}/\hbar\omega_* \simeq (s^2 - 1/4)/(2(q_r l_*)^2) + n + 1/2$, characterized by the angular momentum s around the Rashba-like ring, and the radial harmonic excitations, n , with frequency ω_* . The lowest roton states have $n = 0$, being in real space of the form $\psi_s(\mathbf{r}) \sim e^{is\varphi} e^{-\rho^2/2l_*^2} J_s(q_r \rho)$, with J_s the Bessel function.

The localized states ψ_s are crucial for the dynamics following roton instability. We consider a stable BEC prepared with an initial scattering length $a_i > a_c$. The critical a_c for the onset of instability depends non-trivially on λ and g_d [7]; for the parameters of Fig. 2 it is $a_c = 8.48 a_0$, with a_0 the Bohr radius. We are interested in the instability dynamics after a sudden quench to $a_f < a_c$. Unstable modes lead to a modulational instability characterized by a growing density perturbation $\delta n(\mathbf{r}, t) \equiv n(\mathbf{r}, t) - n_0(\mathbf{r}) \propto \sqrt{n_0(\mathbf{r})} \Re(f_-(\mathbf{r}))$. As for the $\omega = 0$ case, $f_- \simeq (E(q_r)/\epsilon) f_+ \propto \sqrt{n_0(\mathbf{r})} F(\mathbf{r})$. Hence the most unstable roton modes result in a localized modulation at the trap center, $\delta n(\mathbf{r})/n_0(\mathbf{r}) \propto \Re(\psi_s(\mathbf{r}))$.

The most unstable mode is $\psi_0(\mathbf{r})$, but other modes may contribute to the instability due to the small energy difference between low- s levels ($\sim \hbar\omega_*/(q_r l_*)^2$). As a non-trivial consequence of that, the density pattern that develops after the quench is influenced by the initial population of the excitations exponentially amplified during the destabilization. We mimic this dependence by considering a small initial seeding $\phi(\mathbf{r}, t = 0) = \phi_0(\mathbf{r})e^{i\chi(\mathbf{r})}$, where ϕ_0 is the ground-state calculated for a_i , and $|\chi(\mathbf{r})|/\pi < \xi$ is a random phase sampled from a homogeneous uniform distribution with a variable amplitude ξ . Although this allows us to discuss the possible collapse scenarios, the actual amplitude of the initial fluctuations depends on a_i and on the temperature T , and its analysis lies beyond the scope of this Letter [33].

Figures 2 show the results of our simulations of Eq. (1) for an erbium dBEC [34]. For a small initial population of the unstable modes, the modulation instability proceeds at a sufficiently slow pace and $\psi_0(\mathbf{r})$ dominates. As a result, a localized pattern of concentric rings develops (Fig. 2a), in excellent agreement with $\delta n(\mathbf{r})/n_0(\mathbf{r}) \propto \psi_0(\mathbf{r})$, see Fig. 2d. The corresponding momentum distri-

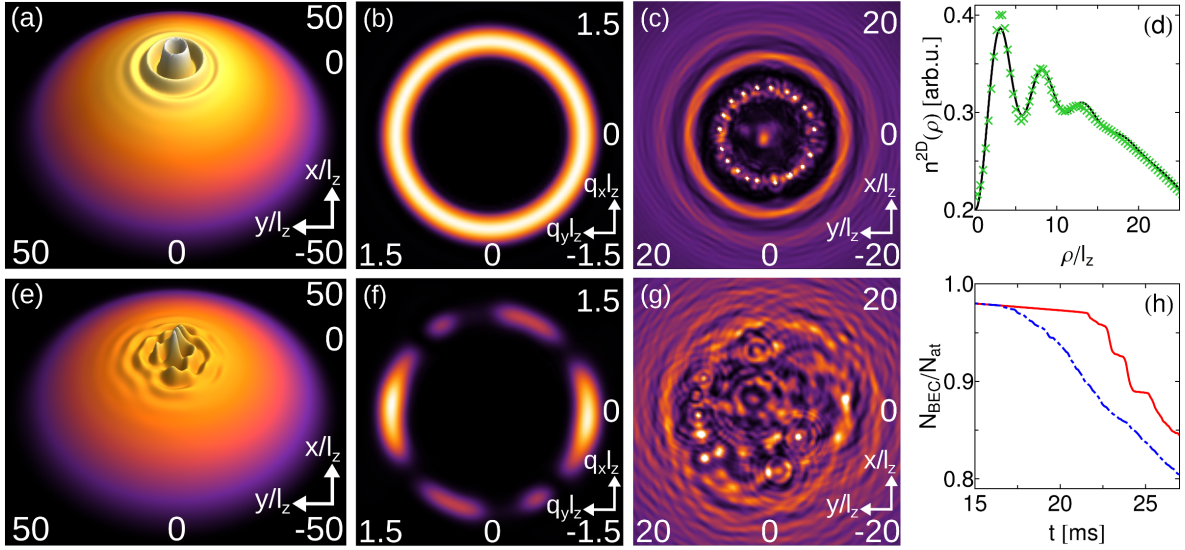


FIG. 2: (Color online) Roton instability for 10^5 Er atoms, with $\omega_z = 2\pi \times 450$ Hz ($l_z \simeq 0.3 \mu\text{m}$), $\lambda = 30$, $a_i = 8.49a_0 > a_c = 8.48a_0$ and $a_f = 0$ (see text). (a) Column density $n^{2D}(\rho) = \int n(\mathbf{r})dz$ showing concentric rings ($s = 0$) formed after $t = 19$ ms for small initial fluctuations ($\xi = 10^{-10}$, see text). (e) Modulational instability after $t = 15.5$ ms consisting of several s states for large initial fluctuations ($\xi = 10^{-6}$, see text). (b) and (f): momentum distribution of (a) and (e) respectively (we have suppressed the large peak at $q = \sqrt{q_x^2 + q_y^2} = 0$). (c) and (g): post-collapse dynamics after $t = 23$ ms for (a) and $t = 19.5$ ms for (e), respectively. (d) Radial cut of (a) (green crosses) and theoretical column density of the form $n^{2D}(\rho) \propto (1 - \rho^2/R^2)^{3/2}(1 + AJ_0(q_r\rho)e^{-\rho^2/2l_*^2})$ (solid black line), with $R \simeq 51l_z$, $A \simeq -0.4$, $q_rl_z \simeq 1.25$, and $l_* = 2^{1/4}(R/q_r)^{1/2} \simeq 7.6l_z$. The value of q_r is calculated using the local spectrum picture. (h) Remnant atoms for the case (a) (solid red line) and (e) (dashed blue line).

bution presents a Rashba-like ring (Fig. 2b) [35]. In contrast, for larger initial fluctuations the pattern growth is too fast to select ψ_0 only, and the created density pattern results from a (shot-to-shot dependent) linear combination of different ψ_s , being characterized by a superposition of eccentric collapse centers (Fig. 2e). The corresponding momentum distribution still presents a ring-like structure but with an azimuthal modulation arising from the linear combination of various ψ_s (Fig. 2f).

The global (phonon-like) collapse studied in chromium and erbium dBECs [3, 36] results in large atom losses and in a d -wave pattern in time-of-flight (TOF) pictures. Remarkably, the roton instability discussed above leads to a very different collapse dynamics. Three-body losses become crucial in the collapse dynamics and we included them by adding $-i\hbar \frac{L_3}{2} N^2 |\phi(\mathbf{r}, t)|^4 \phi(\mathbf{r}, t)$ [36] to Eq. (1), with a loss rate $L_3 = 10^{-28} \text{cm}^{-6} \text{s}^{-1}$. The concentric rings appearing in Fig. 2a eventually undergo a sequential collapse and azimuthal instability, starting from the inner (denser) ones towards the outer ones (Fig. 2c) leading to a step-like atom number decrease (Fig. 2h). The superimposed eccentric collapse centers appearing in Fig. 2e lead to a complex post-collapse behavior with characteristic mutually interfering jets expelled out of each local collapse center (Fig. 2g). In this case the atom decrease is smooth (Fig. 2h). In both scenarios TOF pictures lack the d -wave symmetry, presenting, due to the *local* character of the collapse, a large peak at $q = 0$, with an addi-

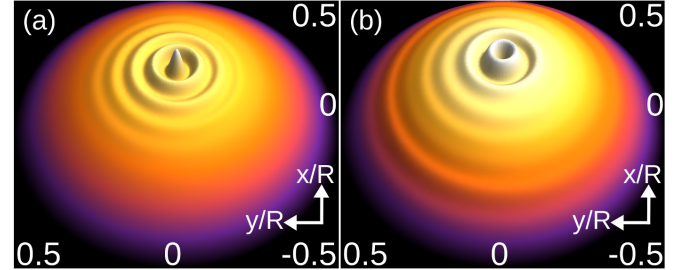


FIG. 3: (Color online) Same parameters as in Fig. 2a but arresting the collapse after 16 ms with a quench of a up to $8.55a_0 > a_c$. Snapshots of the central region right after the quench (a) and 80 ms later (b). Note a clear density modulation confined at the trap center.

tional ring feature during the first collapse stages (see a thorough TOF analysis in the supplementary material). Moreover, the local collapse results in small atom losses, compared to the large losses in global collapses. Roton local collapse can be hence distinguished from the phonon global collapse by the atom losses and the TOF images, even without accessing in-situ dynamics [37].

Interestingly, the roton instability may be used to create a confined roton gas. The density pattern obtained after quenching down to $a_f < a_c$ may be interpreted as the growth of the roton population. At the initial stage of the instability, the roton population is small compared

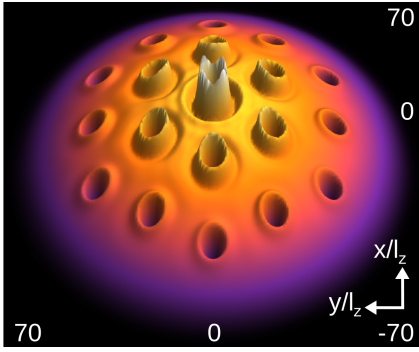


FIG. 4: (Color online) Vortex lattice for a BEC of $N = 10^5$ Er atoms at the threshold of the roton instability. Parameters as in Fig. 1 with a rotational frequency 0.3ω .

to N and we may neglect condensate depletion or roton-roton interactions. Once the roton gas is populated we stabilize it by quenching up to $a > a_c$. Since m_* and ω_* do not vary significantly around the instability threshold, the created rotons (density patterns) remain confined at the trap center after the quench, as shown in Fig. 3.

A deep roton minimum induces close to a perturbation a large susceptibility against the formation of density modulations with the roton wavelength. This well-known effect in He [15–19] is also relevant for dBECs [21]. The local spectrum picture implies a spatially dependent susceptibility, which we illustrate for the case of vortices [38]. Vortex cores present a crater-like shape in the case of a deep roton minimum [20, 21], that disappears when the minimum is shallow or absent. Therefore, vortices at different positions in a trapped BEC present a different core profile. This is shown for a vortex lattice in Fig. 4, where we depict the ground-state of an erbium BEC rotating around the z axis with an angular frequency $\Omega = 0.3\omega$. Note that core modulations at the trap center disappear for vortices at the boundary.

In summary, we have shown that an inhomogeneous trapping in pancake dBECs with large aspect ratios leads to a spatial roton confinement which is crucial to understand the roton instability. The roton dispersion has not yet been observed experimentally, being currently a major goal pursued by several groups. Roton confinement is expected to play a key role in these experiments, since harmonic traps are typically employed and large aspect ratios are needed to study the roton dispersion. In addition to the local susceptibility discussed above [38], roton confinement should be carefully considered when measuring the critical superfluid velocity, performing Bragg scattering [39], or analyzing finite temperature physics, which may be very interesting since the thermal roton cloud is expected to localize at the center of the trap.

We acknowledge funding by the German-Israeli Foundation, and the DFG (SA1031/6 and Exzellenzcluster QUEST).

- [1] A. Griesmaier et al., Phys. Rev. Lett. **94**, 160401 (2005); Q. Beaufils, et al., Phys. Rev. A **77**, 061601 (2008).
- [2] M. Lu et al., Phys. Rev. Lett. **107**, 190401 (2011); M. Lu, N. Q. Burdick, and B. L. Lev, Phys. Rev. Lett. **108**, 215301 (2012).
- [3] K. Aikawa, et al., Phys. Rev. Lett. **108**, 210401 (2012).
- [4] K.-K. Ni, et al., Science **322**, 231 (2008); M. H. G. de Miranda, et al., Nat. Phys. **7**, 502 (2011); A. Chotia, et al., Phys. Rev. Lett. **108**, 080405 (2012).
- [5] C.-H. Wu et al., Phys. Rev. Lett. **109**, 085301 (2012); T. Takekoshi et al., Phys. Rev. A **85**, 032506 (2012).
- [6] T. F. Gallagher and P. Pillet, in Adv. At., Mol., Opt. Phys. **56**, 161 (2008); Robert Löw et al., J. Phys. B: At. Mol. Opt. Phys. **45**, 113001 (2012).
- [7] See M. A. Baranov, Phys. Rep. **464**, 71 (2008); T. Lahaye et al., Rep. Prog. Phys. **72**, 126401 (2009); M. A. Baranov et al., Chem. Rev. **112**, 5012 (2012).
- [8] S. Müller et al., Phys. Rev. A **84**, 053601 (2011)
- [9] L. Pitaevskii and S. Stringari, *Bose-Einstein condensation*, Oxford Univ. Press (New York, 1993).
- [10] L. Santos, G. V. Shlyapnikov, and M. Lewenstein, Phys. Rev. Lett. **90**, 250403 (2003).
- [11] S. Ronen, D. C. E. Bortolotti, and J. L. Bohn, Phys. Rev. Lett. **98**, 030406 (2007).
- [12] L. D. Landau, J. Phys. USSR **11**, 91 (1947); Phys. Rev. **75**, 884 (1949); R. P. Feynman, Phys. Rev. **94**, 262 (1954).
- [13] L. Landau, J. Phys. (Moscow) **5**, 71 (1941).
- [14] R. M. Wilson, S. Ronen, and J. L. Bohn, Phys. Rev. Lett. **104**, 094501 (2010).
- [15] T. Regge, J. Low Temp. Phys. **9**, 123 (1972).
- [16] F. Dalfovo, Phys. Rev. B **46**, 5482 (1992).
- [17] Y. Pomeau and S. Rica, Phys. Rev. Lett. **71**, 247 (1993).
- [18] N. G. Berloff and P. H. Roberts, J. Phys. A **32**, 5611 (1999).
- [19] S. Villerot, B. Castaing, and L. Chevillard, J. Low Temp. Phys. **169**, 1 (2012).
- [20] S. Yi and H. Pu, Phys. Rev. A **73**, 061602(R) (2006).
- [21] R. M. Wilson, S. Ronen, J. L. Bohn, and H. Pu, Phys. Rev. Lett. **100**, 245302 (2008).
- [22] H.-Y. Lu et al., Phys. Rev. A **82**, 023622 (2010).
- [23] R. M. Wilson, S. Ronen, and J. L. Bohn, Phys. Rev. A **80**, 023614 (2009).
- [24] O. W. Dietrich et al., Phys. Rev. A **5**, 1377 (1972); E. C. Svensson, A. D. B. Woods, and P. Martel, Phys. Rev. Lett. **29**, 1148 (1972); P. R. Roach et al., J. Low Temp. Phys. **12**, 375 (1973).
- [25] P. B. Blakie, D. Baillie, and R. N. Bisset, Phys. Rev. A **86**, 021604 (2012).
- [26] I. Iguchi, Phys. Rev. A **6**, 1087 (1972).
- [27] See the supplementary material.
- [28] We assume the BEC away from the narrow regions of biconcave density profiles [11].
- [29] T. D. Stanescu, B. Anderson and V. Galitski, Phys. Rev. A **78**, 023616 (2008).
- [30] S. Sinha, R. Nath, and L. Santos, Phys. Rev. Lett. **107**, 270401 (2011).
- [31] Roton instability was discussed in Ref. [23]. However, roton confinement played no role there, due to the low λ considered. Confinement effects might be however inferred from an unpublished numerical simu-

lation (<http://grizzly.colorado.edu/~bohn/movies/collapse.htm>). In our numerics, we observed localized modulational instabilities for $\lambda \gtrsim 14$.

- [32] Concentric rings were observed by N. G. Parker et al., Phys. Rev. A **79**, 013617 (2009). However, the ring structure was not localized and did not result from roton confinement, but from dynamically unstable phonon modes.
- [33] In our calculations a_i is chosen close to a_c , but its actual value is not relevant, since we just employ the ground-state for $a = a_i$ and add numerical noise. However, the value of a_i may be relevant for the actual fluctuations. If the spectrum is weakly (or not) rotonized for a_i , the initial population of the dominant unstable modes for $a = a_f$ (which are around the roton minimum) is negligible when $k_B T \ll \mu_i(0)$ (k_B is the Boltzmann constant), corresponding to small ξ in Fig. 2. In contrast, the initial population of unstable modes may be significant for $k_B T \sim \epsilon_r$, if the roton depth approaches zero for a_i , corresponding to large ξ in Fig. 2.
- [34] Similar results are expected for other magnetic species.
- [35] Prior to destabilization the dBEC presents a narrow momentum distribution at $q = 0$ with a width $\propto 1/R$. We have removed the $q = 0$ contribution in Figs. 2b and 2f, to highlight the ring-like pattern as well as the azimuthal structure along the ring when several s states are mixed. A thorough analysis of the momentum distribution is performed in the supplementary material.
- [36] T. Lahaye, et al., Phys. Rev. Lett. **101**, 080401 (2008).
- [37] In-situ imaging may be possible in on-going Dy experiments (A. Griesmaier, private communication).
- [38] The local spectrum should also play an important role in the stability spectroscopy of rotons, recently proposed by J. P. Corson, R. M. Wilson, and J. L. Bohn, arXiv:1301.1991. In particular, the collapse will be first induced at the center of the trap, where the susceptibility against density perturbations is the largest.
- [39] Effects of the roton confinement on Bragg spectroscopy may be inferred from some results of Ref. [25]. In particular, the roton confinement leads to a marked uncertainty ($\propto 1/l_*$) in the roton momentum.

SUPPLEMENTARY MATERIAL FOR "ROTON CONFINEMENT IN TRAPPED DIPOLAR BOSE-EINSTEIN CONDENSATES"

DERIVATION OF THE LOCALIZED ROTON WAVE FUNCTIONS

Homogeneous xy case ($\omega = 0$)

We briefly summarize in this subsection the main formalism developed in Ref. [10]. For $\omega = 0$, the ground-

state is of the form $\phi_0(z)e^{-i\mu t/\hbar}$, where μ is the chemical potential and

$$\left\{ -\frac{\hbar^2}{2m} \nabla^2 + \frac{m}{2} \omega_z^2 z^2 + (g + g_d) |\phi_0(z)|^2 - \mu \right\} \phi_0(z) = 0, \quad (4)$$

We assume $(g + g_d) > 0$. For $\mu \gg \hbar\omega_z$ the condensate presents a Thomas-Fermi (TF) density profile, $|\phi_0(z)|^2 = n_0(1 - z^2/L^2)$, with $n_0 = \mu/(g + g_d)$ being the maximum density, and $L = \sqrt{2\mu/m\omega_z^2}$ the TF radius.

Excitations of energy ϵ are evaluated by substituting $\phi(\boldsymbol{\rho}, z, t) = e^{-i\mu t/\hbar} [\phi_0(z) + u(\boldsymbol{\rho}, z)e^{-i\epsilon t/\hbar} - v(\boldsymbol{\rho}, z)^* e^{i\epsilon t/\hbar}]$ (with $\boldsymbol{\rho} \equiv (x, y)$) into the 3D non-local GPE (Eq.(1) of our Letter), and keeping only linear terms in the Bogoliubov amplitudes u and v . For $\omega = 0$, the excitations have a defined in-plane momentum \mathbf{q} , and we may write $f_{\pm}(\boldsymbol{\rho}, z) \equiv [u(\boldsymbol{\rho}, z) \pm v(\boldsymbol{\rho}, z)] = f_{\pm}(z)e^{i\mathbf{q}\cdot\boldsymbol{\rho}}$. The Bogoliubov-de Gennes equations (BdG) read:

$$\epsilon f_- = \frac{\hbar^2}{2m} \left[-\frac{d^2}{dz^2} + q^2 + \frac{\nabla^2 \phi_0}{\phi_0} \right] f_+ \equiv H_{kin} f_+, \quad (5)$$

$$\epsilon f_+ = H_{kin} f_- + H_{int}[f_-], \quad (6)$$

with

$$H_{int}[f_-] = 2(g_d + g)f_-(z)|\phi_0(z)|^2 - (3/2)g_d q \phi_0(z) \times \int_{-\infty}^{\infty} dz' f_-(z') \phi_0(z') \exp(-q|z - z'|). \quad (7)$$

For each q we calculate the eigenenergies. The lowest one, $\epsilon(q)$ builds the dispersion law.

The most interesting behavior occurs for $qL \gg 1$. We may now introduce $f_+(z) = W(z)\phi_0(z)$. Expressing f_- through W from Eq.(5), we substitute it into Eq.(6) and integrate over dz' in $H_{int}[f_-]$ as the main contribution to the integral comes from a narrow range of distances $|z' - z| \sim 1/q$. This yields (here $\chi = z/L$)

$$\hbar^2\omega^2 \left[\frac{1}{2}(1-\chi^2)\frac{d^2}{d\chi^2} - \left(1 + \frac{3}{2(1+\beta)}\right)\chi\frac{d}{d\chi} \right] W(\chi) + \left[\epsilon^2 - E(q)^2 - \frac{2\beta-1}{1+\beta}\mu E(q)(1-\chi^2) - \frac{3\hbar^2\omega^2}{2(1+\beta)} \right] W(\chi) = 0, \quad (8)$$

where $E(q) = \hbar^2 q^2/2m$. Here we omitted terms of the order of $E(q)\hbar^2\omega^2/\mu$ and $\hbar^4\omega^4/\mu^2$, since they are small compared to either $\hbar^2\omega^2$ or $E(q)^2$. For each mode of the confined motion (along the z direction), the solution of Eq.(8) can be written as an expansion series in Gegenbauer polynomials $C_n^\lambda(\chi)$, where $\lambda = (4+\beta)/2(1+\beta)$, and $n \geq 0$ is an integer. For $\mu E(q)|2\beta-1|/(1+\beta) \lesssim \hbar^2\omega^2$ the lowest solution is of the form $W(\chi) \simeq 1 + \sum_{n>0} a_n C_n^\lambda(\chi)$, with small amplitudes a_n of Gegenbauer polynomials of higher order, while the lowest-eigenenergy (and hence the dispersion) is given by

$$\epsilon_h^2(q, \mu) = E(q)^2 - G(\beta)E(q)\mu + \hbar^2\omega_z^2, \quad (9)$$

with $G(\beta) \equiv \frac{(\beta-2)(5\beta+2)}{3(1+\beta)(2\beta+1)}$.

Trapped xy case

We consider in the following $\omega > 0$, with $\lambda = \omega_z/\omega \gg$

1. Due to the xy confinement, we cannot employ any-

more a plane wave basis for the Bogoliubov amplitudes, as we did above. However, we assume that: (i) the Bogoliubov amplitudes are, in momentum space, strongly peaked around a momentum $q \gg 1/R$; and (ii) the Bogoliubov amplitudes are localized at the center of the trap, in a region with a radius much smaller than R . These assumptions must be checked self-consistently, but we anticipate that they are fulfilled for a sufficiently large aspect ratio $\lambda \gg 1$. If this is the case, we may proceed as for the homogeneous case, but taking into account that (a) the chemical potential is now ρ dependent, and (b) the Bogoliubov amplitudes are not plane waves anymore. Assuming the above conditions are met, we may write $f_+(\boldsymbol{\rho}, z) \simeq F(\boldsymbol{\rho})W(x)\phi_0(\boldsymbol{\rho}, z)$ (now $x^2 = \rho^2/R^2 + z^2/L^2$), where the function $F(\boldsymbol{\rho})$ has a narrow momentum distribution $F(\mathbf{q})$ peaked at q_r with a momentum width $\delta q \propto 1/l_* \ll q_r$ and $\phi_0(\boldsymbol{\rho}, z)$ is the ground-state. Taking into account (a) and (b), we re-write Eq. (8) in the form

$$\hbar^2\omega^2 \left[\frac{1}{2}(1-x^2)\frac{d^2}{dx^2} - \left(1 + \frac{3}{2(1+\beta)}\right)x\frac{d}{dx} \right] W(x)F(\boldsymbol{\rho}) + \left[\epsilon^2 - E(\hat{\mathbf{q}})^2 - \frac{2\beta-1}{1+\beta}\mu E(\hat{\mathbf{q}})(1-x^2) - \frac{3\hbar^2\omega^2}{2(1+\beta)} \right] W(x)F(\boldsymbol{\rho}) = 0, \quad (10)$$

where $\hat{\mathbf{q}} \equiv -i\nabla$. The lowest energy eigenstates still fulfill $W(x) \simeq 1$, but now we must keep explicitly the spatial dependence of $F(\boldsymbol{\rho})$.

$$\epsilon^2 F(\boldsymbol{\rho}) = [E(\hat{\mathbf{q}})^2 - G(\beta)E(\hat{\mathbf{q}})\mu(\rho) + \hbar^2\omega_z^2] F(\boldsymbol{\rho}) \quad (11)$$

Expanding around the roton minimum in the local spectrum, and moving to momentum space ($\boldsymbol{\rho} = i\nabla_q$) we obtain

$$\epsilon^2 \tilde{F}(\mathbf{q}) = \left[\epsilon_r + \frac{\hbar^2(q-q_r)^2}{2m_*} - \frac{1}{2}m_*\omega_*^2\nabla_q^2 \right]^2 \tilde{F}(\mathbf{q}) \quad (12)$$

where $\tilde{F}(\mathbf{q})$ is the Fourier transform of $F(\boldsymbol{\rho})$. Hence $\tilde{F}(\mathbf{q})$ are the eigenstates of the hamiltonian $\hat{H} \equiv \frac{\hbar^2(q-q_r)^2}{2m_*} -$

$\frac{1}{2}m_*\omega_*^2\nabla_q^2$, which may be calculated as discussed in the Letter.

Density modulations

Note that density modulations are given by the f_- amplitudes, in the form: $\delta n(\mathbf{r}, \mathbf{t}) \equiv n(\mathbf{r}, t) - n_0(\mathbf{r}) \propto \sqrt{n_0(\mathbf{r})}\Re(f_-(\mathbf{r}))$, where \Re denotes real part. For the $\omega = 0$ case, and since $W(\chi) \simeq 1$, then from Eq. (5) one obtains that $f_- \simeq (E(q)/\epsilon)f_+$. For the $\omega > 0$ case, since $W(x) \simeq 1$ still, and we assume that $\tilde{F}(\mathbf{q})$ is narrowly peaked around q_r , we obtain the same result for the trapped case. Hence apart from a constant $f_-(\mathbf{r}) \propto f_+(\mathbf{r}) \propto \psi_0(\mathbf{r})F(\boldsymbol{\rho})$. As a result: $\delta n(\mathbf{r}, \mathbf{t}) \propto$

$$n_0(\mathbf{r})\Re(F(\boldsymbol{\rho})).$$

TIME-OF-FLIGHT PICTURES

Although the most straightforward way of studying roton confinement is of course given by in-situ measurements, time-of-flight (TOF) pictures are expected to show a clear difference as well, when compared to the cloverleaf pattern characteristic of the phonon collapse (as observed in chromium [36] and, more recently, in erbium [3]). More specifically, TOF pictures may reveal clear traces of the Rashba-like ring characterizing the localized roton-like excitations.

Due to the fast expansion after release, TOF pictures are expected to reproduce well the in-situ momentum distribution at the time of releasing. We have calculated the momentum distribution of the condensate at different stages during the instability dynamics. Our results for the same case studied in Fig. 2(a) of the main text are depicted in Fig. 5, where we show both the column density on the q_x - q_y plane (i.e. integrated along q_z), and that on the q_x - q_z plane (i.e. integrated along q_y). We show in particular the results obtained during the first stages of the collapse dynamics. For the parameters of Fig. 2(a) of the main text, the Rashba-like ring is clearly visible during the first stages of the collapse, being later on destroyed due to the subsequent collapse of the spatial ring-like density modulations. As a result the ring TOF pattern is washed out. In later stages TOF pictures are characterized by the appearance of large momentum excitations on the xy plane (induced by the collapse of the

local rings) which becomes visible in the q_x - q_z distribution as pronounced jets along x .

The low-momentum peak always appears saturated in our pictures. It was eliminated from Figs. 2b and 2g of the main text, since we were only interested in showing the Rashba-like feature in momentum space. The large low-momentum peak is the result of two effects. The first one is purely geometric. The $q = 0$ peak is always relatively strong, since it is not spread in the angular variable φ (as it is the ring feature discussed above). The second reason is more physical, and it is linked with the local nature of the collapse. Since only a small fraction of the atoms is actually participating in the modulational instability and in the subsequent collapse, a large fraction of atoms remains at low momentum. Note that the low momentum peak also broadens due to the generation of low energy phonons during the collapse. As a result, the low-momentum peak dominates the TOF pictures. This is in itself a clear difference with respect to the phonon collapse, where the initial low-momentum peak transforms into a cloverleaf pattern due to the global nature of the collapse.

However, although the relative number of particles produced in the Rashba-like ring may be small, the actual absolute number of particles may be certainly sizable. In Fig. 5 (lower panel) we depict at various times the number of particles at different radial momenta. This plot shows that a significant number of particles is found in the ring before the ring feature is eventually washed-out (up to 1500 particles at 21.5 ms).

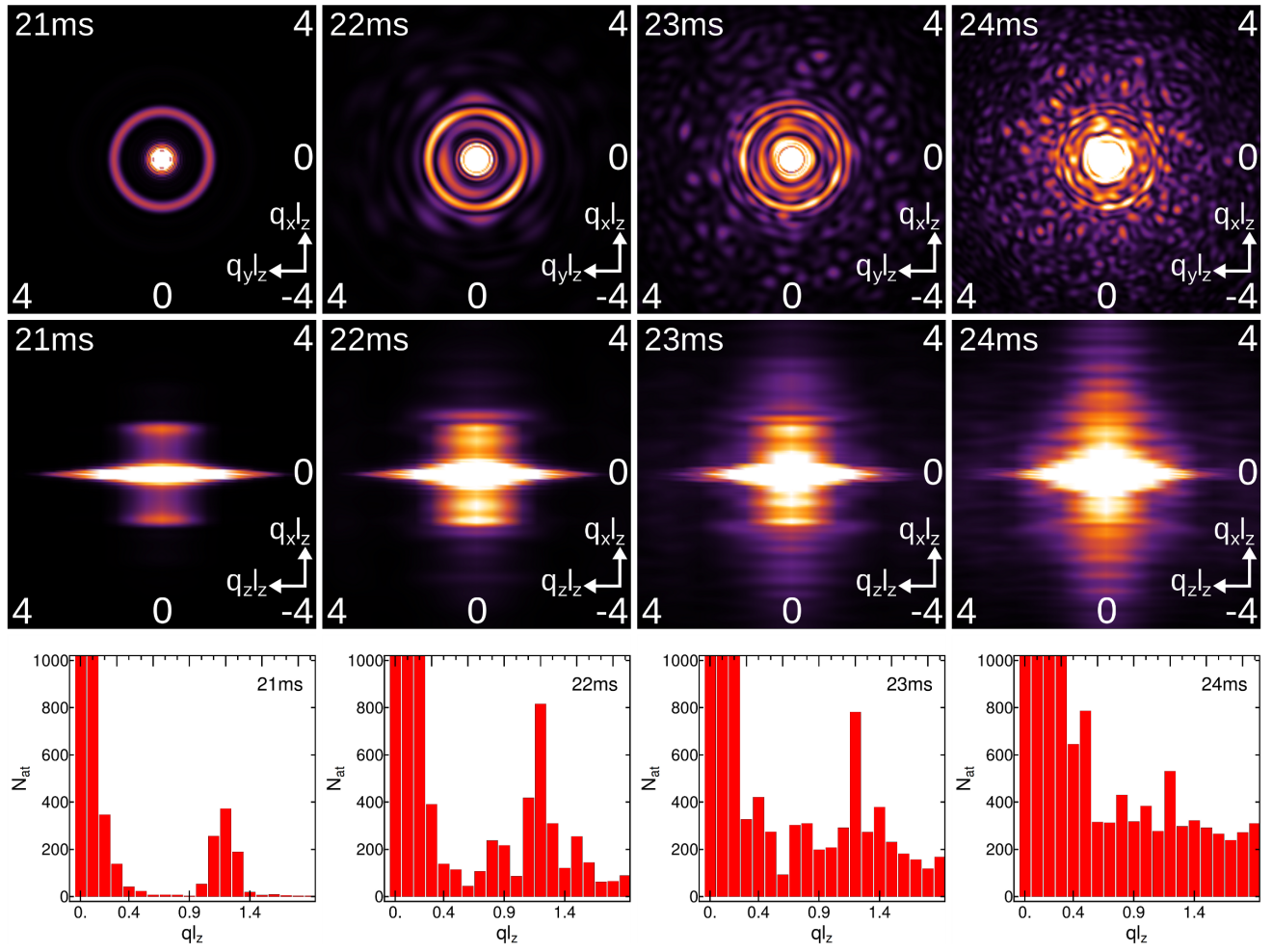


FIG. 5: (Color online) Momentum distribution for different times for the same case depicted in Fig. 2(a) of the main text, as it would be revealed by a TOF experiment. In the upper panel we show the q_x, q_y momentum distribution (integrated over q_z) and in the middle panel the q_x, q_z momentum distribution (integrated over q_y). The lower panel shows the integrated population at different intervals of the radial momentum $q = \sqrt{q_x^2 + q_y^2}$.